ADVANCED FUNCTIONAL MATERIALS
www.afm-journal.de

Mechanomorphogenic Films Formed via Interfacial Assembly of Fluorinated Amino Acids

*Janna N. Sloand, Tyler E. Culp, Nichole M. Wonderling, Enrique D. Gomez, and Scott H. Medina**

Nature has evolved several elegant strategies to organize inert building blocks into adaptive supramolecular structures. Favored among these is interfacial self-assembly, where the unique environment of liquid–liquid junctions provides structural, kinetic, thermodynamic, and chemical properties that are distinct from the bulk solution. Here, antithetical fluorous–water interfaces are exploited to guide the assembly of non-canonical fluorinated amino acids into crystalline mechanomorphogenic films. That is, the nanoscale order imparted by this strategy yields self-healing materials that can alter their macro-morphology depending on exogenous mechanical stimuli. Additionally, like natural biomolecules, organofluorine amino acid films respond to changes in environmental ionic strength, pH, and temperature to adopt varied secondary and tertiary states. Complementary biophysical and biochemical studies are used to develop a model of amino acid packing to rationalize this bioresponsive behavior. Finally, these films show selective permeability, capturing fluorous compounds while allowing the free diffusion of water. These unique capabilities are leveraged in an exemplary application of the technology to extract perfluoroalkyl substances from contaminated water samples rapidly. Continued exploration of these materials will advance the understanding of how interface-templated and fluorine-driven assembly phenomenon a can be co-utilized to design adaptive molecular networks and living matter.

1. Introduction

Molecular self-assembly is a powerful tool for the design of biomimetic, designer scaffolds. It enables otherwise inanimate molecules to create functional structures with unique biochemical properties that emerge through hierarchical organization. Inception of this nanoscale order is often driven via interfacial self-assembly, where physisorption of biomolecules at liquid–liquid interfaces initiates the growth of supramolecular architectures. Such interfacial processes are theorized to have been fundamental to the emergence of life by templating organic primordial compounds into bioactive higher order structures.[1] Liquid–liquid separation continues to be a conserved paradigm for cellular organization in modern organisms as well. For example, phase separation of intrinsically disordered proteins gives rise to membraneless organelles that play fundamental roles in mammalian physiology and disease.[2–5] Emerging evidence suggests the protein condensation that precedes organelle development is driven at the amino acid level, where the morphology of separated phases correlates to molecular repeats and residue identity.[6–9] Phenylalanine plays a particularly prominent role in directing interfacial protein condensation.[10–12] Given the amino acid-centric nature of these coacervate processes, non-canonical amino acids evoke particular interest due to their ability to alter organelle phase separation in ways not yet accessible by nature. Among these, fluorine-containing amino acids are a privileged class of non-canonical building blocks that exploit the presence of fluorine to drive unique assembly phenomena.[13]

Inspired by this, we set out to explore the interfacial assembly of non-canonical perfluorinated amino acids at fluorous–water interfaces. We focus on 9-fluorenylmethyloxycarbonyl-L-phenylalanine (Fmoc-Phe) derivatives as the assembly constituent. This is based on the well-established propensity for Fmoc-Phe amino acids, as well as Fmoc-functionalized aromatic peptides,[14–17] to organize into fibrillar supramolecular architectures.[18–23] To create the fluorous organelle, we utilize perfluorocarbon (PFC) solvents that form well-defined phases in water, ideally suited to template the assembly of fluorinated

Dr. J. N. Sloand, Prof. S. H. Medina
Department of Biomedical Engineering
The Pennsylvania State University
University Park, PA 16802, USA
E-mail: shm126@psu.edu
Dr. T. E. Culp, Prof. E. D. Gomez
Department of Chemical Engineering
The Pennsylvania State University
University Park, PA 16802, USA
N. M. Wonderling
Materials Characterization Laboratory
The Pennsylvania State University
University Park, PA 16802, USA
Prof. E. D. Gomez
Department of Materials Science and Engineering
The Pennsylvania State University
University Park, PA 16802, USA
The ORCID identification number(s) for the author(s) of this article can be found under https://doi.org/10.1002/adfm.202104223.

DOI: 10.1002/adfm.202104223

Fmoc-Phe derivatives. We show that addition of perfluorinated Fmoc-Phe, referred to as Fmoc-F_5-Phe, to fluorous liquid–liquid systems yields mechanomorphogenic films that change their macro-morphology depending on the mechanical stimulus provided. These thin films form at air–water or fluorous–water interfaces and demonstrate dynamic and self-healing behavior. Through a series of biochemical and biophysical assays we probe the mechanistic basis for these emergent material properties and delineate the structure-activity relationships that govern their bioresponsive capabilities. Finally, we demonstrate the utility of these materials to purify water samples of perfluoroalkyl substances (PFAS) rapidly and efficiently. PFAS compounds are now recognized as dangerous water contaminants by the US Environmental Protection Agency, which urgently require remediation technologies to ensure clean and safe drinking water.[24–27] Therefore, these dynamic materials hold tremendous promise for the development of abiotic bioremediation strategies, in addition to their potential to advance bioinspired protocells and smart drug-delivery systems.

2. Results and Discussion

2.1. Fluorous Film Formation and Optimization

Fluorous amino acid films are prepared by pipetting a solution of perfluorohexane (PFHx) containing Fmoc-F_5-Phe (20 mmol L^{-1}) into ultrapure water, leading to the spontaneous supramolecular organization of the amino acid at the fluorous–water interface (**Figure 1**A, step i). This irreversible step initiates the oligomerization process to form an opaque fluorous organelle. Mechanical agitation leads to hierarchical reorganization of the oligomers to produce a thin film at the air–water interface (Figure 1A, i → ii). The resultant mechanomorphogenic material responds dynamically to an external mechanical stimulus. For example, an applied centrifugal force disassembles the film to produce amorphous precipitates (ii → iii), which can be spontaneously reassembled if exposed again to air (iii → ii). Conversely, if the disassembled material is subjected to an ultrasonic stimulus (e.g., ultrasound) it will revert back to the parent fluorous organelle (iii → iv), which if agitated will again reorganize into a thin film at the air–water interface (iv → ii). Fluorous film disassembly and reassembly can be actuated using standard laboratory equipment (Movie S1, Supporting Information) and can be performed cyclically without compromising the integrity of the hierarchical film. The opacity of the interfacial film also enables optical density (OD_{600}) measurements to be used to distinguish the disassembled and reassembled states (Figure 1B).

Multiparametric optimization identified that a 200 µL injection volume of the Fmoc-F_5-Phe loaded PFHx solution produced the thickest, and thus most optically dense, films (Figure 1C). Saturating the system with excess fluorous material (volumes > 200 µL) reduced the competency of the films and favored the formation of macroscopic emulsions in water (Figure S1, Supporting Information). Varying the amount of Fmoc-F_5-Phe in PFHx demonstrated a critical film concentration of 5 mmol L^{-1}, with increasing amino acid content generally yielding more optically dense films up to 50 mmol L^{-1} (Figure 1D; Figure S2, Supporting Information). Concentrations above this threshold produced unstable films that quickly precipitated if further perturbed. Therefore, 20 mmol L^{-1} Fmoc-F_5-Phe concentrations were prioritized for all further studies.

How the hydrophobicity of the non-aqueous phase impacts film competency was next evaluated using various hydrocarbon and fluorocarbon solvents (Figure 1E). Polar hydrocarbon liquids, defined by partition coefficients (log*P*) ≤2.3, were not able to form the well-defined boundary layer necessary to initiate interfacial film formation. In some cases, these polar solutions instead generated macroscopic hydrogels (Figure S3, Supporting Information). Conversely, all four PFCs tested were sufficiently immiscible in water (log*P* 5.1–9.9) to produce supramolecular films (Figure S4, Supporting Information). In fact, we found an inverse correlation between PFC solution density and film competency (Figure S5, Supporting Information), suggesting that increasing the film weight by using denser PFCs negatively impacts the structural stability of the film. Taken together, our data indicates that generation of Fmoc-F_5-Phe films requires a well-defined fluorous phase with the aqueous environment, and that amino acid concentration and PFC volume must be counterbalanced to drive the kinetic equilibrium of assembly toward interfacial film formation over emulsification.

2.2. Structure-Function-Performance Relationships of Fluorous Films

Evidence suggests that assembly of disordered proteins at liquid–liquid interfaces is driven by intermolecular interactions between bulky, hydrophobic amino acids.[28,29] With this in mind, we surveyed the ability of Fmoc-containing Val (V), Ile (I), Leu (L), Phe (F), Tyr (Y), and Trp (W) residues to form supramolecular films comparable to Fmoc-F_5-Phe (F_5-F) (**Figure 2**A; Figure S6, Supporting Information). Fmoc-Ala (A) and Fmoc-Gly (G) were included as negative controls given their lack of bulky beta branched or aromatic side chains. As expected, non-fluorinated Fmoc-Phe (F) underwent interfacial assembly to form competent films. Surprisingly, Fmoc-Gly (G) was able to form an initial quasi-stable film in the PFHx-water system as well (Figure S6, Supporting Information, panel B). One possible explanation is that the lack of a sterically bulky side chain on the Gly residue enables Fmoc-driven hydrophobic assembly to take place. However, the absence of further stabilizing effects, for example additional π–π stacking of phenyl side chains, prevents the long-term stability of this transient state. Taken together, this suggests that the combination of the fluorenyl (Fmoc) and phenyl (Phe) groups are required for the stable hierarchical assembly of interfacial fluorous films.

While both Fmoc-Phe and Fmoc-F_5-Phe were found to share the same critical assembly concentration (5 mmol L^{-1}; Figure 1D; Figure S7, Supporting Information), there was a marked difference in their macroscopic behavior (Figure 2B). For example, Fmoc-Phe films form a uniformly flat 2D sheet, while Fmoc-F_5-Phe films are characterized by an ability to fold on itself and form undulations. This may be explained by the significant difference in supramolecular grain size between the two films (Figure 2C). Fmoc-F_5-Phe grains (31.4 ± 17.9 µm)

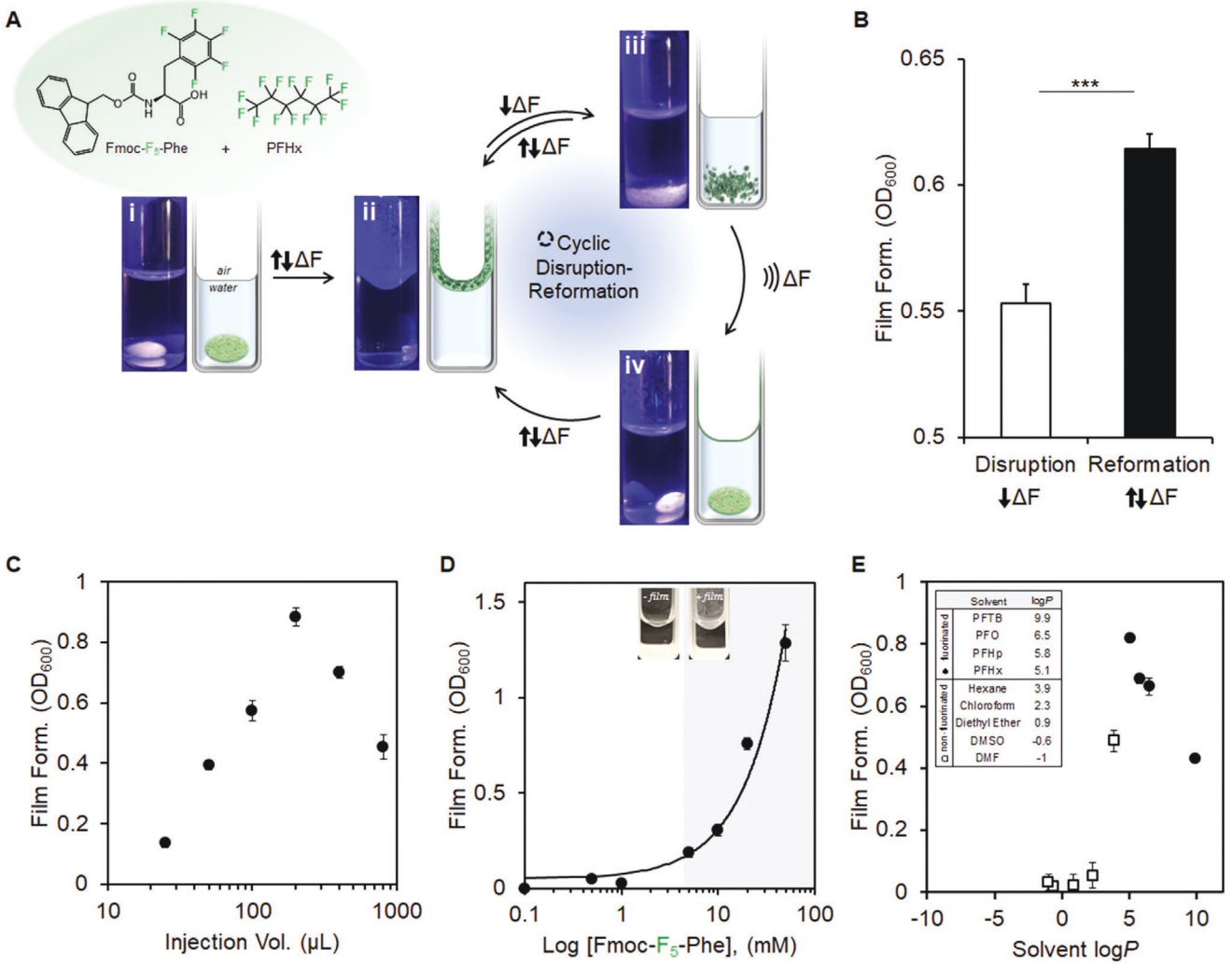

Figure 1. Functional behavior and optimization of Fmoc-F_5-Phe films. A) Schematic and UV optical images of mechanomorphogenic films formed via supramolecular assembly of Fmoc-F_5-Phe at the perfluorohexane (PFHx)-water interface. Step i shows formation of initial fluorous organelle encompassed by the self-assembled film. Exposure to air leads to spontaneous re-organization of the film at the air–water interface (step ii). Centrifugal agitation precipitates the film (step iii), which reverts to the assembled macrostate if re-exposed to air (iii → ii). Alternatively, sonication of the precipitated film converts the material back to the initial fluorous organelle (iii → iv). These operations can be performed cyclically ad infinitum. B) Optical density (OD_{600}) of Fmoc-F_5-Phe films in either the disassembled (disrupted, open bars) or reassembled (reformation, black bars) state after 10 disruption-reformation cycles. Statistical significance indicated by *** $p < 0.0001$. C) Density of Fmoc-F_5-Phe films (20 mmol L^{-1}) as a function of varied PFHx injection volume. D) Concentration-dependency of Fmoc-F_5-Phe film formation. Gray region specifies Fmoc-F_5-Phe concentrations that yield competent films (see inset for optical images). E) Competency of Fmoc-F_5-Phe films following assembly in solvent-water systems prepared using various fluorocarbon (●) and hydrocarbon (□) solvents. Film formation (OD_{600}) is plotted as a function of solvent hydrophobicity (log*P*). Data in (B–E) shown as mean ± standard deviation for $n \geq 9$ replicates per condition.

are nearly two times longer than that of Fmoc-Phe (16.5 ± 3.9 μm) and are comparatively more heterogenous. This increased persistence length of Fmoc-F_5-Phe grains may impose folding of the material to relieve the tangential compression force applied by gravity. More importantly, these observations suggest that fluorinated and non-fluorinated Fmoc-Phe amino acid derivatives form monolithic assemblies that are distinct in their hierarchical arrangement.

To test this assertion, we further probed the self-assembled structure of Fmoc-Phe and Fmoc-F_5-Phe interfacial films using fluorescence spectroscopy. Here, the intrinsic fluorescence of the Fmoc moiety can be used to monitor the environment of the fluorenyl excimer during assembly. Results in Figure 2D and Figure S8, Supporting Information, show that Fmoc-F_5-Phe films display a unique feature in the emission spectra at 420–480 nm, which is indicative of extensive J-aggregate formation.[30] The manifold nature of this broad peak (see arrows in Figure 2D) suggests a diverse ensemble of extended J-aggregate morphologies, further supported by the varied supramolecular grain sizes observed in the film (Figure 2C). Similar J-aggregation observed during Fmoc-Phe-Phe assembly[30] provides a possible model for the molecular organization of Fmoc-F_5-Phe. In particular, molecules may be organized in an anti-parallel arrangement, where fluorenyl moieties form alternate β-sheets

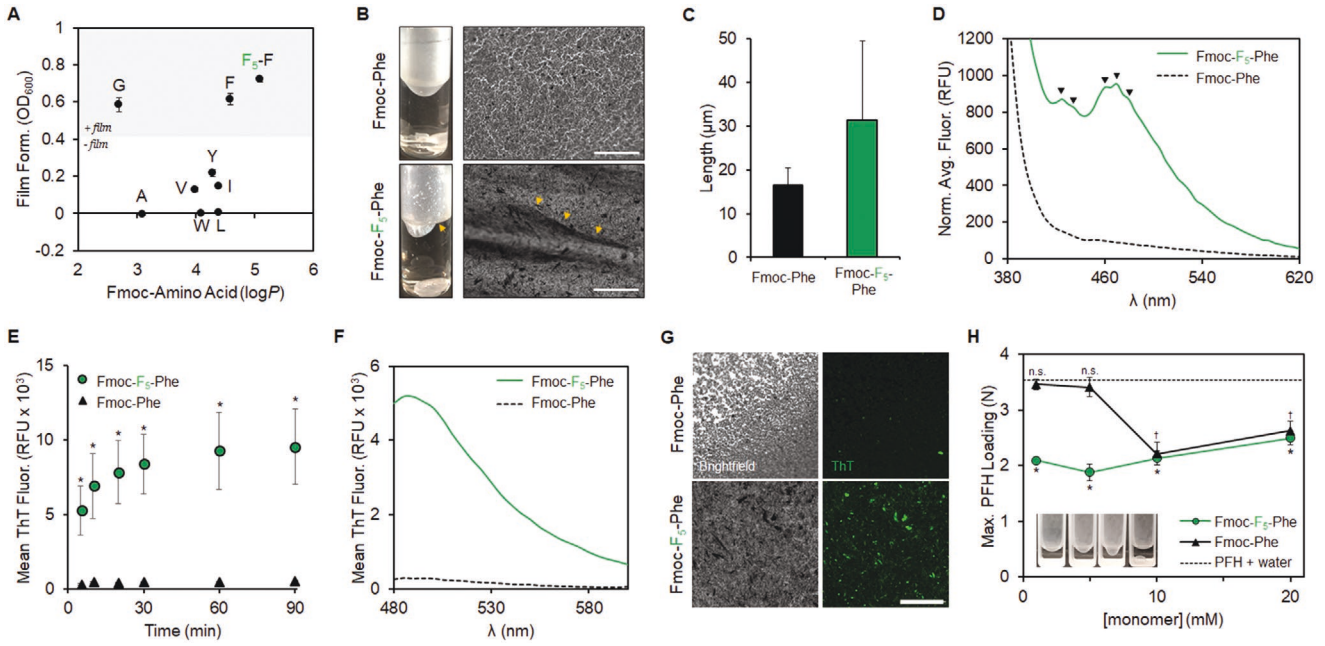

Figure 2. Molecular and structural characterization of fluorous films. A) Film formation of select Fmoc-protected amino acids (20 mmol L^{-1}) in PFHx. Film competency (OD_{600}) plotted versus amino acid hydrophobicity (log*P*) ($n = 9$). B) Optical and brightfield micrographs of Fmoc-Phe and Fmoc-F_5-Phe fluorous films. Yellow arrows indicate surface undulations. Scale bar = 500 µm. C) Comparison of grain length in Fmoc-Phe (black) or Fmoc-F_5-Phe (green) films ($n = 150$). D) Fluorescence emission spectra of Fmoc-Phe and Fmoc-F_5-Phe films ($\lambda_{ex} = 280$ nm, $n = 3$). Results normalized to air controls and reported as relative fluorescence units (RFU). The symbol ▼ highlights multimodal emission peaks unique to Fmoc-F_5-Phe films. E) Mean fluorescence of ThT-labeled Fmoc-Phe and Fmoc-F_5-Phe films as a function of time ($\lambda_{ex} = 450$ nm, $\lambda_{em} = 482$ nm, $n = 3$). Statistical significance determined relative to Fmoc-Phe films; $^{*}p < 0.01$. F) Averaged fluorescence spectra of ThT-labeled Fmoc-Phe and Fmoc-F_5-Phe films at $t = 90$ min ($\lambda_{ex} = 450$ nm, $n = 3$). G) Brightfield and fluorescent micrographs of ThT-labeled Fmoc-Phe and Fmoc-F_5-Phe films. Scale bar = 500 µm. H) Maximum supported load, in newtons (N), of PFHx delivered to the surface of Fmoc-Phe or Fmoc-F_5-Phe air–water films. Statistical significance determined relative to control (PFHx + water) and indicated by $^{\dagger,*}p < 0.01$ for Fmoc-Phe or Fmoc-F_5-Phe, respectively (n.s. = not statistically significant, $n = 3$). Inset, representative optical images of PFHx loading and rupture of Fmoc-F_5-Phe films. Data in (A), (C), (E), and (H) shown as mean ± standard deviation.

to create π-stacked pairs with interleaved fluorinated phenyl rings.[30] It is expected that a second Fmoc-F_5-Phe stack would position itself next to the first one but staggered by one amino acid to allow for interlocking of fluorenyl groups to satisfy π–π interactions. Consecutive layering of these stacked assemblies is expected to yield crystalline micro-sheets, an assertion later validated through electron microscopy. This supramolecular arrangement would likely be directed by favored fluorine–fluorine interactions, where desolvation of perfluorinated phenyl rings provides a strong driving force for supramolecular sequestration within the material bulk. The lack of J-aggregate emissive peaks (>420 nm) for Fmoc-Phe control films further supports this working model of a fluorine-driven assembly phenomena unique to Fmoc-F_5-Phe (Figure 2D). To rigorously test the premise that Fmoc-F_5-Phe assembles into β-sheet rich conformations we subsequently investigated the secondary structure of the film constituents using thioflavin T (ThT). This cationic dye displays a strong enhancement of fluorescence upon binding to β-sheet structures.[31] As expected, substantial ThT fluorescence was observed for Fmoc-F_5-Phe films, but not the nonfluorinated Fmoc-Phe analogue (Figure 2E–G). Collectively, our data demonstrates that the perfluorinated nature of Fmoc-F_5-Phe enables its privileged assembly at fluorous interfaces to form β-sheet rich architectures, while nonfluorinated Fmoc-Phe collapse into amorphous oligomers at the liquid–liquid interface.

Given their dissimilar nano-scale morphologies, we next asked the question whether Fmoc-F_5-Phe and Fmoc-Phe films display differential assembly phenomena at the air–water interface. We hypothesized that the fluorous nature of Fmoc-F_5-Phe would promote its organization at the water surface and therefore more potently decrease surface tension relative to Fmoc-Phe. To test this, we designed a mechanical assay to quantify the maximum force required to rupture films residing at the air–water interface. Here, PFHx droplets were incrementally added at increasing volumes to the top of the film until the material failed. The maximum weight of the PFHx droplet that could be supported, as a function of amino acid concentration, was then recorded and results compared to the native surface tension of water as a control (Figure 2H). At low amino acid concentrations (1–5 mmol L^{-1}) only Fmoc-F_5-Phe showed a significant decrease in water surface tension, presumably due to its preferred assembly at the air–water interface. Conversely, Fmoc-Phe required higher concentrations (≥10 mmol L^{-1}) to perturb surface tension. Interestingly, during these experiments we observed that, although the films resist the passive transfer of PFC droplets, aqueous solutions freely pass through the material (Figure S9, Supporting Information). Additionally, the films can be stably deposited onto various plastic, metallic, and glass solid support media where they act as superhydrophobic coatings (Figure S10, Supporting Information). These observations, together, suggest interfacially templated

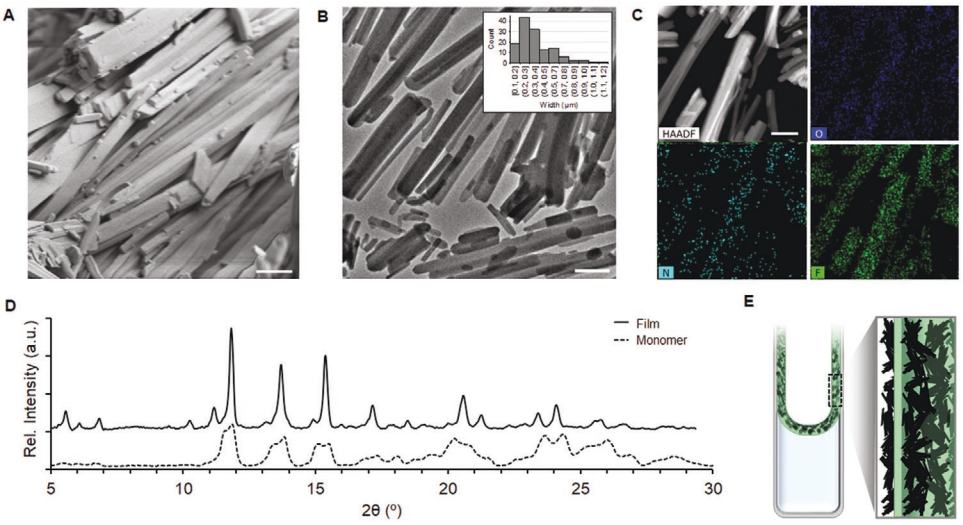

Figure 3. Nanoscale investigation of Fmoc-F_5-Phe crystalline packing. Representative A) scanning and B) bright-field transmission electron microscopy (SEM/TEM) images of self-assembled Fmoc-F_5-Phe structures. Panel (B) inset, histogram of fibril width ($n \geq 120$). C) High-angle annular dark-field (HAADF) scanning TEM imaging and energy-dispersive X-ray spectroscopy (EDS) elemental analysis of Fmoc-F_5-Phe assemblies (O, N, F). D) X-ray diffractogram of Fmoc-F_5-Phe pre- (monomer, dashed line) and post-assembly into supramolecular films (Film, black line). E) Schematic showing the proposed tri-layer assembly of Fmoc-F_5-Phe films formed at the air–water interface. Here, sheets of crystalline Fmoc-F_5-Phe assemblies (black) float on either side of a thin PFC liquid interior (green). Scale bars in (A–C) are 1 µm.

Fmoc-F_5-Phe films may show selective permeability and thus be utilized for membrane or chromatographic separation processes; an assertion we affirm in later perfluoroalkyl contaminant capture studies.

To better understand the hierarchical structure of Fmoc-F_5-Phe films the needle-like assemblies were isolated and electron microscopy performed. Scanning electron micrographs shown in **Figure 3**A demonstrate that Fmoc-F_5-Phe assembles into stacked sheets that laminate to form micron-sized crystalline plates (additional images in Figure S11, Supporting Information). Bright-field transmission electron microscopy (TEM) images shown in Figure 3B suggest these structures possess a solid core, are uniform in density, and heterogenous in width (389 ± 201 µm, see Figure 3B inset). High-angle annular dark-field scanning TEM (HAADF) imaging paired with energy-dispersive X-ray spectroscopy (EDS) elemental mapping confirm these assemblies are made entirely from fluorine-rich Fmoc-F_5-Phe amino acids, as opposed to a co-assembly with the PFHx solvent (Figure 3C; Figure S12, Supporting Information).

Notably, the prismatic architecture of these Fmoc-F_5-Phe structures is in striking contrast to other Fmoc-Phe or Fmoc-Phe-Phe self-assembled systems, which typically adopt nanoscale ribbon,[30] hollow tube,[32] or fibrillar morphologies.[18,19,33] The notable exception is Fmoc-NPhe peptoid analogues reported by Nilsson and coworkers, which adopt crystalline states in DMSO-water systems.[18] However, crystallization occurs slowly (upward of 1 month to evolve micron-sized crystals) and produce amorphous precipitates in solution. In contrast, here we show that, provided a sufficiently fluorous interface, Fmoc-F_5-Phe amino acids can be templated in their organization to form crystalline plates nearly instantaneously. Comparing powder X-ray diffraction (PXRD) profiles for Fmoc-F_5-Phe films and the monomeric starting material provides further structural insights (Figure 3D). PXRD revealed sharper intensity peaks for assembled Fmoc-F_5-Phe films in comparison to the broad peaks present for the monomeric starting material. Peak width is inversely proportional to crystallite size, therefore, peak sharpening observed for the films is indicative of Fmoc-F_5-Phe organization into larger crystallites (33.4 ± 10.2 nm) compared to the monomer (16.2 ± 11.0 nm). While this supports a supramolecular crystalline architecture for Fmoc-F_5-Phe films, a uniform crystal lattice structure could not be deconvoluted from the spectrum. This suggests that Fmoc-F_5-Phe orients into a manifold of different crystal lattice systems, with this morphology likely a consequence of the rapid organization induced by interfacial assembly. These results also provide further insight into the multiple Fmoc emission peaks observed during fluorescence spectroscopy performed on Fmoc-F_5-Phe films (Figure 2D).

Combining the findings from these biophysical studies allows us to develop an early mechanistic hypothesis of Fmoc-F_5-Phe film evolution. During the initiation phase, amphiphilic Fmoc-F_5-Phe amino acids likely partition to the fluorous–water interface via interpolation of the perfluorinated phenyl ring into the PFC solvent. Hypothetically, this would orient Fmoc-F_5-Phe in such a way to generate a unimolecular 2D sheet with fluorenyl and carboxyl moieties extended into the aqueous solvent. Hydrophobic adsorption of additional Fmoc-F_5-Phe molecules could nucleate the growth of a second sheet via π–π interactions between interlocking fluorenyl groups. This would subsequently expose a highly fluorinated surface available for continued addition of Fmoc-F_5-Phe amino acids via fluorine–fluorine interactions. Repetition of this process could reasonably construct the laminated 3D crystalline architectures observed in SEM and TEM imaging (Figure 3A,B). This would ultimately yield a multilayered film, where the crystalline Fmoc-F_5-Phe assemblies organize on both surfaces of the perfluorocarbon liquid interior layer (Figure 3E). This working

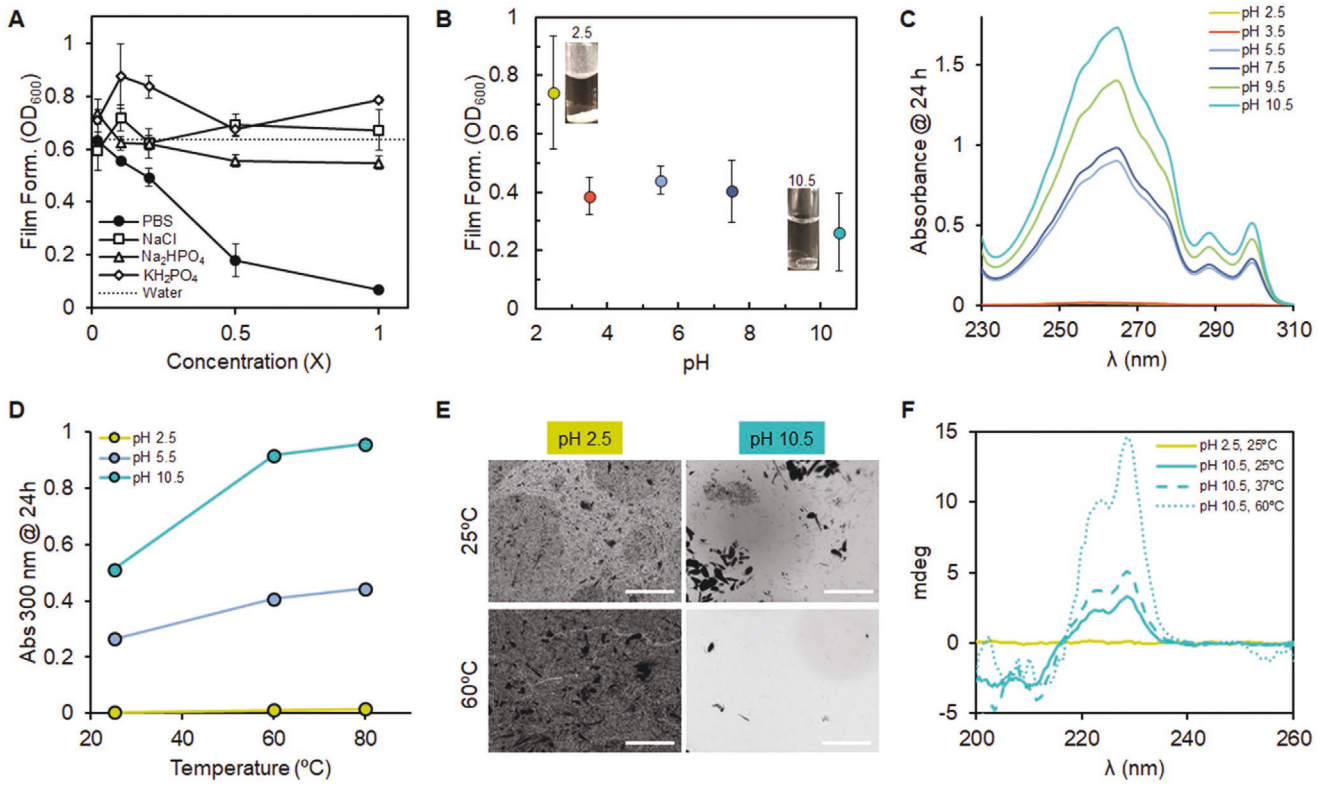

Figure 4. Environmental adaptability of Fmoc-F_5-Phe films. A) Influence of media ionic strength on Fmoc-F_5-Phe film competency (20 mmol L^{-1} amino acid). Data shown relative to 1X concentration of PBS and includes the complete buffered solution as well as three independent salt components. Dashed line represents OD_{600} of films formed in unbuffered water as a control. B) pH-dependency on Fmoc-F_5-Phe film formation following a 24 h assembly time in water at the indicated pH. Inset, representative optical images of film samples assembled at pH 2.5 or 10.5. Data in panels (A) and (B) shown as mean ± standard deviation (n = 9). C) Representative absorbance spectra of soluble Fmoc-F_5-Phe fraction in pH 2.5 – 10.5 water. D) Absorbance (λ = 300 nm, Fmoc characteristic peak) of soluble Fmoc-F_5-Phe fraction in pH 2.5 (yellow), 5.5 (blue), and 10.5 (aqua) water, following a 24 h incubation at 25–80 °C. E) Brightfield optical micrographs of Fmoc-F_5-Phe films at the air–water interface following assembly at pH 2.5 or 10.5 and exposed to 25 or 60 °C conditions for 24 h. Scale bar = 500 µm. F) Representative circular dichroism spectra of films at the air–water interface formed under varying pH and temperature conditions.

model is supported by our prior microscopic imaging of the films showing plate-like structures floating on a liquid surface (Figure 2B; Figure S4, Supporting Information). Further, the lack of free PFHx droplets following complete film assembly confirms the fluorous solvent is incorporated into the final material (Figure S2, Supporting Information).

2.3. Environmental Film Responsiveness

Nilsson and coworkers previously demonstrated the importance of the C-terminal carboxylate on the assembly of Fmoc-Phe derivatives.[19,33] These studies established the role of ionic strength and pH in modulating the Coulombic repulsion between anionic charged molecules and promoting assembly of various Fmoc-Phe analogues. Complementary studies have also shown that Fmoc-Phe hydrogels display altered mechanical and optical properties following annealing of the assemblies at elevated temperatures.[34] Therefore, we sought to understand how all three of these stimuli (i.e., ionic strength, pH, temperature) effect the interfacial assembly of Fmoc-F_5-Phe films (**Figure 4**). In the first experiment, Fmoc-F_5-Phe films (20 mmol L^{-1} of amino acid) were assembled in a phosphate buffered solution (PBS) and optical density (OD_{600}) measurements collected to monitor film competency. Results in Figure 4A show that exposure of the films to PBS dramatically reduced their integrity. However, this effect appeared to require the full combination of salts in the PBS formulation. For example, Fmoc-F_5-Phe films exposed to each of the three individual PBS salt components (NaCl, Na_2HPO_4, KH_2PO_4) showed little change in optical density relative to unbuffered water, and under some conditions increased in material opacity (Figure 4A; Figure S13, Supporting Information). This suggests that both Na^+ and K^+ counter ions are required to sufficiently screen the charge and alter the solubility of anionic Fmoc-F_5-Phe molecules to shift its kinetic equilibrium away from self-assembly.

Parallel studies investigated the pH-dependency of film formation following initiation in pH 2.5–10.5 water solutions (Figure 4B). At all pHs tested we observed initial assembly of Fmoc-F_5-Phe films (Figure S14, Supporting Information), but only pH 2.5 maintained an opaque film at the air–water interface up to 3 days post assembly (Figure 4B; Figure S15, Supporting Information). Conversely, films formed at pH 10.5 rapidly deteriorated, and at 24 h the amino acid was predominately dissolved in the alkaline solution. This indicates that removal of intermolecular Coulombic repulsion via protonation

of the Fmoc-F_5-Phe carboxylate (calculated pKa = 2.9) under acidic conditions promotes its assembly at the fluorous interface. Conversely, ionization of the amino acid improves its aqueous solubility, as demonstrated by the monotonic increase in UV–vis absorbance of the Fmoc group (λ = 300 nm) detected in the water layer as pH increases (Figure 4C; Figure S16, Supporting Information).

Finally, thermal stability of the film was investigated at temperatures above the bulk boiling point of PFHx (bp = 57 °C). This is intended to evaluate potential reorganization of Fmoc-F_5-Phe films upon removal of the PFHx interior layer. Film stability is assessed in these experiments at three different initiation pH (2.5, 5.5, 10.5) and indirectly measured as a function of temperature by quantifying the relative amount of the fluorenyl group remaining in the water solution via UV–vis spectroscopy (λ = 300nm) 24 h after assembly. As expected, the concentration of Fmoc-F_5-Phe in water increased as a function of both temperature and pH for films formed at pH > 2.5 (Figure 4D; Figure S17, Supporting Information). No significant dissolution of the amino acid monomer was observed for pH 2.5 films, even at temperatures above the boiling point of PFHx. In fact, microscopy images shown in Figure 4E demonstrate that pH 2.5 films subjected to annealing at 60 °C show a highly compact grain morphology. The appearance of fissures in the film also suggests that removal of the PFHx interior liquid layer increases the brittleness of the material (see pH 2.5 at 60 °C image in Figure 4E), which was subsequently confirmed by its loss of self-healing behavior after annealing. Last, circular dichroism (CD) spectroscopy was performed on the water samples to evaluate the assembly behavior of Fmoc-F_5-Phe dissolved in the aqueous fraction. It has been previously shown that Fmoc-Phe derivatives display characteristic CD features at 200–230 nm indicative of n–π^* transitions of phenyl side chains.[19,35] These same features were observed for aqueous Fmoc-F_5-Phe solutions at pH 10.5, but not pH 2.5 (Figure 4F). This is expected, given that the amino acid is predominately encumbered within the air–water interfacial film under these acidic conditions (Figure 4B), and therefore undetectable in the water layer. Increasing temperature yielded a corresponding increase in the intensity of Fmoc-F_5-Phe spectral features of pH 10.5 solutions. Although precise structural conclusions cannot be drawn from the data, our CD results are consistent with published findings indicating fibril formation of Fmoc-Phe derivatives in aqueous media.[19,35] This suggests that, under alkaline conditions, Fmoc-F_5-Phe amino acids may be forming proto-fibrillar oligomers in water, which if concentrated could potentially assemble into fibrillar arrangements. We explore this potentially new packing modality, and the utility of the resultant thin films for separation processes, in follow up water contaminant capture applications.

2.4. PFAS Capture Using Fmoc-F_5-Phe Films

The fluorine-rich nature of Fmoc-F_5-Phe films encourages their use as capture technologies for perfluorinated compounds. Poly- and PFAS are attractive candidates given their focus as regulated water contaminants by the Environmental Protection Agency (EPA).[24] PFAS are a family of synthetic chemicals utilized as surfactants in a variety of industries (e.g., automotive, electronics, construction), and often enter surface and groundwater systems from manufacturing waste run-off.[25,26] Evidence suggests 97% of Americans have been exposed to these chemicals, which persist and accumulate for long periods of time in the body and can cause adverse health effects.[36–40] This has urged innovation of new PFAS removal technologies that can be readily integrated into existing water treatment infrastructure.

With this need in mind, we coated polystyrene surfaces with Fmoc-F_5-Phe films and evaluated their PFAS capture efficiency (**Figure 5**). Given spectroscopy data suggesting oligomeric assembly of Fmoc-F_5-Phe in alkaline conditions (Figure 4F), we prepared two capture films: one in which films prepared at pH 2.5 were directly deposited onto the plastic substrate by removing the water support layer, and second in which Fmoc-F_5-Phe dissolved in pH 10.5 water was evaporated to gradually deposit the assemblies onto the plastic surface. Intriguingly, this thermal deposition procedure produced two completely different film morphologies (Figure 5A). Fmoc-F_5-Phe films deposited on polystyrene at pH 2.5 look morphologically similar to those at the air–water interface (Figure 2G) and retain their β-sheet rich structure (see fluorescent micrograph in Figure 5A). In contrast, Fmoc-F_5-Phe oligomers in pH 10.5 solutions display concentration-driven self-assembly as the water layer is evaporated. This yields fibrous morphologies which do not positively stain for β-sheet structure using ThT. Ultimately, this confirms that Fmoc-F_5-Phe organize into distinct supramolecular arrangements when driven to assemble at either fluorous interfaces (pH 2.5) or in the bulk aqueous environment (pH 10.5). Based on their dissimilar structural phenotypes we elected to test both material morphologies for contaminant removal applications.

Three perfluoroalkyl sulfonate and carboxylate compounds—perfluorooctanesulfonic acid (PFOS), perfluorooctanoic acid (PFOA), and perfluorononanoic acid (PFNA) (see structures in Figure 5B)—were selected for capture studies based on their regulation under the Safe Drinking Water Act.[24] These studies required us to develop a novel ThT-based PFAS detection assay. We found that the altered ionization state of PFAS compounds following their interaction with the anionic films led to unreliable results using standard mass spectrometry techniques. As an alternative, we hypothesized that ThT may electrostatically complex with each of the three anionic PFAS compounds to enable fluorescence-based detection. Indeed, addition of the fluorophore to each of the three PFAS test solutions resulted in a significant increase in intensity and red-shift of the ThT emission peak, which could be used to generate linear calibration curves for PFOS, PFOA, and PFNA (Figure S18, Supporting Information). Although this assay has a limit of detection well above that of mass spectrometry, to our knowledge this new detection method is the first to allow PFAS analysis using facile fluorescence-based methods. We are exploring development of this diagnostic test in follow up work to analyze PFAS contaminated flows in a rapid and point-of-use manner.

With this detection method in hand, we coated polystyrene support substrates with Fmoc-F_5-Phe films formed under pH 2.5 or pH 10.5 conditions and treated PFOA, PFOS, or PFNA contaminated water solutions for 24 h. Uncoated polystyrene

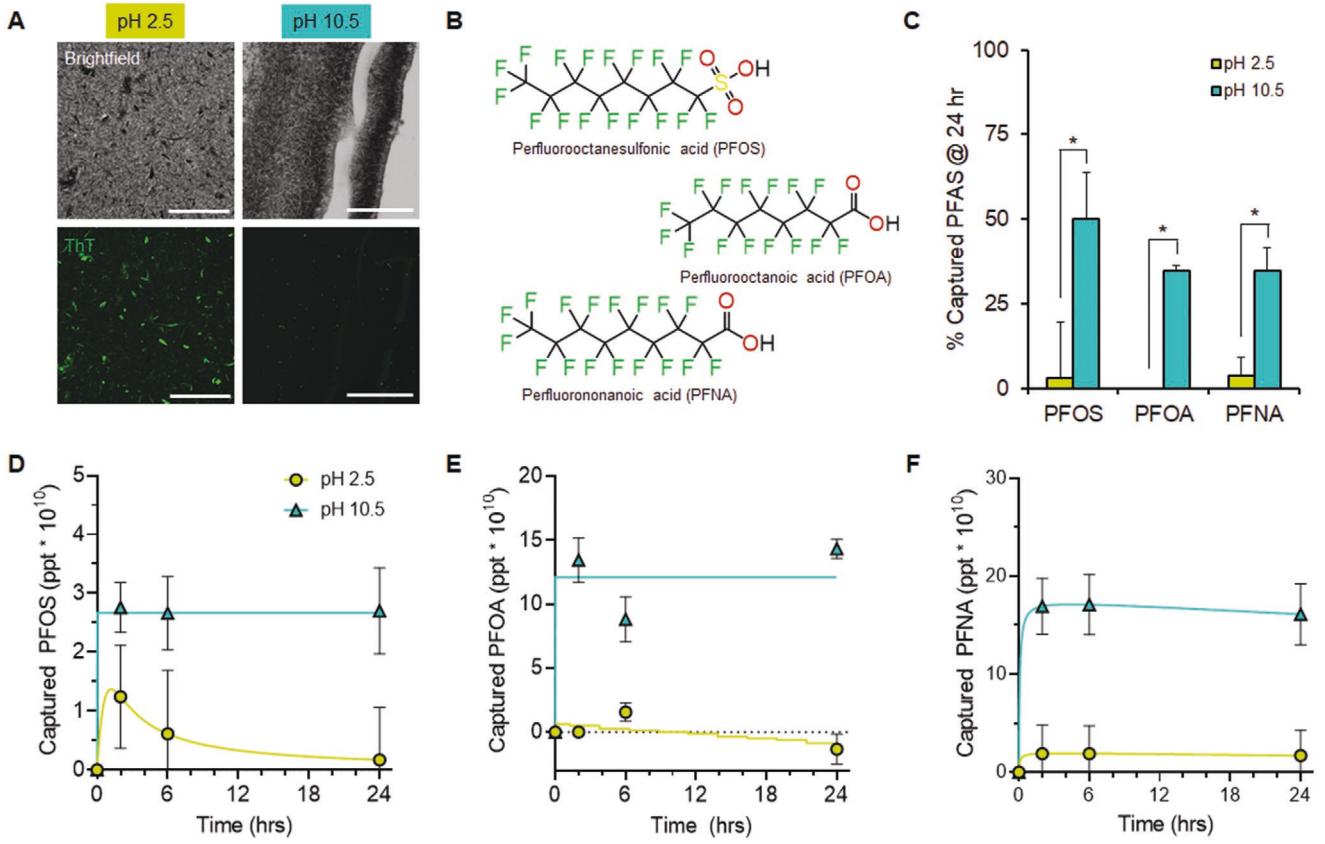

Figure 5. PFAS capture efficiency of Fmoc-F_5-Phe films. A) Brightfield (top) and fluorescent (bottom) micrographs of dried Fmoc-F_5-Phe films prepared at pH 2.5 or 10.5, and stained with ThT. Scale bars = 500 µm. B) Chemical structure of PFAS water contaminants. C) Percent of each PFAS contaminant captured using pH 2.5 and 10.5 films following a 24 h treatment interval. PFOS, PFOA, and PFNA initial concentrations are 0.1, 1, and 1 mmol L^{-1}, respectively. Statistical significance is indicated by $*p < 0.001$. D–F) Kinetics of PFAS capture by Fmoc-F_5-Phe films at 0–24 h for PFOS (D), PFOA (E), and PFNA (F). Data in (C–F) is shown as mean ± SEM ($n = 3$).

was used as a control, which showed minimal non-specific adsorption of the tested PFAS compounds (Figure S19, Supporting Information). All PFAS capture data reported was subsequently normalized to control samples of film in blank water. Results show pH 10.5 prepared Fmoc-F_5-Phe films captured 10–15 times more PFAS contaminants compared to pH 2.5 coatings after a 24 h treatment period, achieving a 35–50% overall capture efficiency (Figure 5C). Similar removal efficiencies have been reported following short term use (≤24 h) of ion exchange, physisorption, and thermal PFAS treatment technologies.[41–44] One explanation for the significant difference in PFAS capture performance between pH 10.5 and 2.5 films may come from their dissimilar secondary structures (Figure 5A). The highly organized, sheet-rich architectures observed within pH 2.5 films may sequester the fluorinated phenyl ring of Fmoc-F_5-Phe within the material bulk. We discuss this packing arrangement in detail above. Conversely, films prepared at pH 10.5 possess a sheet-deficient secondary structure. This amorphous arrangement may more effectively expose fluorinated amino acid side chains to the aqueous environment to facilitate PFAS adsorption.

Follow up experiments monitoring PFAS capture kinetics show that pH 10.5 Fmoc-F_5-Phe films rapidly extract up to 2.5 – 15 × 10^{10} ppt of the contaminants in less than 2 h, and are able to retain the captured molecules for up to 24 h (Figure 5D–F, see polystyrene control data in Figure S20, Supporting Information). It is to be noted that the EPA has set a health advisory level of 70 ppt for PFOA and PFOS in drinking water.[24] This concentration is orders of magnitude below those utilized in our experiments, which were necessitated by the limit of detection of our ThT assay. As a result, we hesitate to comment on the utility of these films for drinking water purification, which is the focus of on-going work. However, there are several industries in which manufacturing waste flows routinely reach PFAS concentrations ≥10^6 ppt.[45,46] This suggests that Fmoc-F_5-Phe films may function as physio-chemical adsorbers suited to primary remediation of highly PFAS contaminated industrial waste.

3. Conclusion

Several approaches have been developed to design supramolecular materials using aromatic amino acid building blocks. Conventional strategies rely on assembly in bulk solution, yielding diverse nanostructures that include spherical particles,[13,47] fibers,[18–20,33] and tubes.[32] This hierarchical diversity, along with their chemical simplicity and tunable intermolecular

associations, have made ultra-short peptides attractive soft matter platforms for biosensing, tissue engineering, and drug delivery applications.[47] Here, we exploit privileged fluorine–fluorine interactions to guide fluorinated amino acid assembly at liquid–liquid interfaces. Understanding how interfacial assembly phenomenon generates dynamic supramolecular scaffolds provides an opportunity to design adaptive matter. As an example, we show that Fmoc-F_5-Phe can be templated to assemble into sheet rich, crystalline films that dynamically respond to diverse mechanical stimuli and adapt to their environment (e.g., ionic strength, pH, temperature), together highlighting their potential as "smart" materials. In particular, we utilize their pH-responsive behavior to test how supramolecular organization influences their molecular capture of PFAS compounds. Proof-of-concept studies show that promoting Fmoc-F_5-Phe to assemble into β-sheet deficient fibrillar structures favors PFAS capture efficiency, presumably due to increased aqueous exposure of the fluorinated phenyl ring. On-going work is focused on optimizing film formulation to achieve PFAS capture efficiencies at, or better than, granulated activated carbon standards (≈95%).[24] That said, a unique advantage of our self-assembled films over current technologies is their mechanomorphogenic nature, which may allow recyclability during PFAS capture applications. For example, saturated films could be dissolved in alkaline solutions to remove captured PFAS, followed by thermal deposition of recovered Fmoc-F_5-Phe to regenerate the virgin material. Incorporating defluorinating microbes into multi-lamellar structures is another exciting avenue of future research. Degradation of PFAS chemicals by engineered microbes represents an emerging and attractive bioremediation strategy. However, this approach currently requires long time scales for efficient contaminant remediation (≈100 days).[48,49] Utilizing Fmoc-F_5-Phe films to locally concentrate PFAS contaminants for microbial remediators may significantly enhance degradation kinetics. These applications highlight the potential of organofluorine scaffolds to serve as next generation biomaterials, which exploit the fluorous effect to expand the design landscape of supramolecular self-assembled materials with unique and adaptive biofunctionalities.

4. Experimental Section

Materials: Fmoc-pentafluoro-L-phenylalanine, Fmoc-tyrosine, and *N*,*N*-dimethylformamide were purchased from Chem Impex. Fmoc-L-phenylalanine, Fmoc-alanine, Fmoc-glycine, Fmoc-valine, Fmoc-tryptophan, Fmoc-isoleucine, and Fmoc-leucine were purchased from CEM. Perfluorohexane, perfluoroheptane, perfluorooctane, and perfluorotributylamine were purchased from Oakwood Chemical. Perfluorooctanoic acid and perfluorononanoic acid were purchased from TCI Chemical, and perfluorooctanesulfonic acid was purchased from Matrix Scientific. Thioflavin T and dimethyl sulfoxide spectrophotometer grade were purchased from Alfa Aesar. Phosphate buffer saline 1X was purchased from Corning. Hexane and sodium chloride were purchased from Fisher Chemical. Diethyl ether, chloroform, and potassium monophosphate were purchased from Acros Organics. Sodium diphosphate was purchased from VWR.

Film Preparation: Air–water interface films were formed using Fmoc-F_5-Phe dispersed into PFHx via 30 s sonication. The Fmoc-F_5-Phe/PFHx mixture was injected into 3 mL deionized (DI) water in a glass vial with the pipette tip fully submerged. Film was initiated by shaking the closed vial up and down for >10 s allowing for the air–water interface film to form. Cyclic disruption–reformation starts by manually centrifuging the vial until the film precipitates. Sonication for 2–5 s promotes condensing precipitates into a PFHx dense film bubble which can form an air–water interface film again by shaking for >10 s. Vials with films were optically imaged using a UV light source.

Optical Density: Optical density (OD_{600}) was measured to quantify film formation based on its opacity. Films were formed in 800 µL water in a 1 cm path quartz cuvette by injecting 100 µL of Fmoc-F_5-Phe/PFHx, parafilming the cuvette top, and initiating film formation. Absorbance at 600 nm was measured immediately following film formation with the light path going through the film/air layer using an Agilent UV–vis spectrometer. Injection volume was 100 µL and Fmoc-F_5-Phe concentration was 20 mmol L^{-1} in PFHx, unless specified otherwise. Each film sample was measured for absorbance with three internal replicates using 800 µL ultrapure water as a blank. Mean film formation (OD_{600}) was calculated per film condition and reported as mean ± standard deviation for $n \geq 3$.

Mechanical Characterization: Fmoc-F_5-Phe and Fmoc-Phe films were prepared by pipetting 100 µL of each amino acid at 1–50 mmol L^{-1} concentrations in PFHx into 800 µL of pH 2.5 water in a glass vial. After complete film formation, PFHx was added dropwise (5 µL) ≈ 1–2 mm directly above the film layer at a rate of six drops per minute until reaching failure, as indicated by excess PFHx pinching off to form a bubble. Total number of PFHx drops until failure (x) were counted and calculated for maximum PFHx loading ($x - 1$). Total weight of PFH held at the air–water interface was calculated by: F (N) = mg and $m = ((x - 1) \times 5\ \mu L + 100\ \mu L) \times 10^{-3} \times d$, where d is the density of PFHx (d = 1.643 g mL^{-1}). All conditions were reported as mean ± standard error of the mean (n = 3). Optical images were captured during the dropwise addition of PFHx.

Fluorescence Spectroscopy and Microscopy: Films were prepared in a 12-well microplate with 100 µL injection of 20 mmol L^{-1} Fmoc-F_5-Phe/PFHx or Fmoc-Phe/PFHx into 1–2 mL pH 2.5 water. Fluorescence emission spectra were measured using BioTek Cytation3 microplate reader. For J-aggregate analysis, samples were excited at 280 nm and scanned for emission from 310–600 nm. Resulting spectra were normalized to water control and averaged, reported as normalized average fluorescence for n = 3. For β-sheet analysis, 25 µL of 1 mmol L^{-1} thioflavin T (ThT) in water was added to the film water layer. Samples were shaken at 100 rpm for 5 min, and then excited at 450 nm and scanned for emission at 480–700 nm at timepoints t = 0, 5, 10, 20, 30, 60, and 90 min. Mean ThT fluorescence (λ_{em} = 482 nm) was calculated per timepoint for each film and reported as mean ± standard deviation (n = 3). Resulting spectra were analyzed for mean ThT fluorescence and reported for t = 90 min. All ThT data was normalized to film samples without ThT.

For fluorescent microscopy, Fmoc-F_5-Phe and Fmoc-Phe films were prepared with 200 µL injected into 2 mL DI water in a 12-well plate. After film initiation, 50 µL of 1 mmol L^{-1} ThT in water was added to the film water layer. Samples were shaken at 100 rpm for 5 min, and then films were imaged via brightfield and GFP filter cube on BioTek Cytation 3 multimodal plate reader. Film fibril length was calculated using ImageJ and reported as average length ± standard deviation for n = 150 for each condition.

Electron Microscopy: Fmoc-F_5-Phe films were prepared with 200 µL injected into 3 mL pH 2.5 water in 12-well plate and then dip coated onto a metal SEM stub with double sided carbon tape. Dried samples were sputter coated with Au/Pd 60:40 using a Capovani Brothers Bal-tec SCD-050 sputter coater and imaged using a Zeiss SIGMA VP-FESEM using secondary electron imaging.

For transmission electron microscopy and scanning transmission electron microscopy, Fmoc-F_5-Phe films were prepared with 200 µL injected into 3 mL pH 2.5 water in a glass vial and then were dip coated onto a carbon wafer and embedded into epoxy and sectioned via microtome. Samples were imaged using a Talos F200X transmission electron microscope. Z-contrast imaging was done using a high angle annular dark field (HAADF) detector operating in STEM mode with a 1 µs dwell time and 160 mm camera length. Elemental analysis was

performed by electron dispersive X-ray spectroscopy (EDS) via HAADF-STEM. Film fibril width was calculated using ImageJ and reported as average width ± standard deviation for $n \geq 120$.

Powder X-Ray Diffraction: Data was collected on a Malvern Panalytical XPert Pro MPD theta-theta diffractometer (1.5406 Å wavelength, 45 kV, 40 mA). For film sample, Fmoc-F_5-Phe films in pH 2.5 water were deposited onto a zero-background silicon holder via dip coating and set to dry overnight before analysis. Fmoc-F_5-Phe powder was taken directly from the stock for analysis serving as a pre-film control. All samples were scanned from 5.01–29.97 at step size 0.026° and plotted at relative intensity. Samples were analyzed using OriginPro software for diffractogram smoothing and baseline correction, and for crystallite size analysis.

UV–Vis and Circular Dichroism Spectroscopy: Fmoc-F_5-Phe films were formed in vials containing 3 mL water at pH 2.5–10.5 and incubated for 24 h at 25, 60, or 80 °C. Films were optically imaged and then 200 µL sample of the water layer was aliquoted into a 1 cm path quartz cuvette and measured for absorbance from 200–800 nm using Agilent UV–vis spectrometer. All data as normalized to water only with representative spectra reported.

Circular dichroism (CD) spectroscopy was performed on the film water layer. Fmoc-F_5-Phe/PFH (20 mmol L^{-1}) was injected into 2 mL of pH 2.5, 5.5, or 10.5 water in a 12-well plate and incubated at 25, 37, or 60 °C for 24 h. Samples from the film water layer were aliquoted (200 µL) into a 1 mm path length quartz cell, and sample measurements were taken using a Jasco-J1500 circular dichroism spectrometer. Representative spectra were reported for each condition.

Per- and Poly-Fluoroalkyl Detection by ThT: A thioflavin T (ThT) detection method for perfluorooctanoic acid, perfluorooctanesulfonic acid, and perfluorononanoic acid in water was developed. PFOA (1 mmol L^{-1}), PFOS (100 µmol L^{-1}), or PFNA (1 mmol L^{-1}) were dissolved in water by vortexing and sonicating. Absorbance scan from 200–800 nm was performed for all PFAS compounds ± 25 µmol L^{-1} ThT and ThT alone over timepoints $t = 0$–20 min. Peak absorbances were determined as 410, 369, and 415 nm for PFOA, PFOS, and PFNA, respectively, and used as excitation wavelengths (λ_{ex}). Calibration curves for each were analyzed for fluorescence emission with peak emissions (λ_{em}) at 550, 530, and 525 nm for PFOA, PFOS, and PFNA, respectively. All data was normalized to ThT only serving as negative control (Figure S18, Supporting Information).

For PFAS capturing experiments, films were formed using 20 mmol L^{-1} Fmoc-F_5-Phe in pH 2.5 or 10.5 water in 12-well plates and dried down to be supported on the bottom of the well plate. Solutions of PFOA, PFOS, or PFNA were added directly into the well ± film. Timepoint samples (200 µL) were collected at $t = 0$, 2, 6, and 24 h. For each sample, 195 µL was aliquoted into a 96-well black bottom plate, and then 5 µL of ThT (1 mmol L^{-1}) was added at $t = 0$. The plate was shaken at 100 rpm for 10 min and assessed for remaining PFAS via ThT method as described above (PFOA $\lambda_{ex}/\lambda_{em}$ 410/550 nm, PFOS $\lambda_{ex}/\lambda_{em}$ 369/530 nm, and PFNA $\lambda_{ex}/\lambda_{em}$ 415/525 nm). All film + PFAS samples were normalized to film + water controls. Remaining concentration of PFAS was analyzed using calibration curve and then captured concentration was calculated: $[PFAS]_{initial} - [PFAS]_{remaining}$ and converted from mM to ppt and averaged. Mean captured PFAS (ppt × 10^{10}) was reported for all timepoints as mean ± standard error of the mean for $n = 3$.

Statistical Analysis: Data was normalized to control sample as specified. All data is reported as mean ± standard error of the mean (SEM). Statistical significance was determined using one-tailed Student's *t*-test where *p*-values ≤ 0.05 were reported as statistically significant.

Supporting Information

Supporting Information is available from the Wiley Online Library or from the author.

Acknowledgements

The authors acknowledge and thank the Penn State Microscopy and Cytometry Facility–University Park, PA for use of circular dichroism instrumentation. The authors also acknowledge the Penn State Materials Characterization Laboratory–University Park, PA for use of the electron microscopy instrumentation and assistance with powder X-ray diffraction. Funding for this research was provided by the NSF Faculty Early Career Development Program (CAREER) to S.H.M. under award number DMR-1845053. J.N.S. acknowledges funding support from the Penn State Graduate Research Fellowship. T.E.C. and E.D.G. acknowledge funding support from NSF through DMR-1905550.

Conflict of Interest

The authors declare no conflict of interest.

Author Contributions

J.N.S. and S.H.M. conceived the hypothesis and designed the research. J.N.S. performed experiments with assistance of T.E.C. and N.M.W. in specialized instrumentation and analysis. J.N.S. and S.H.M. interpreted the data and wrote the manuscript. T.E.C., N.M.W., and E.D.G. contributed to writing of the manuscript. S.H.M. and E.D.G. contributed to resources.

Data Availability Statement

The data that support the findings of this study are available from the corresponding author upon reasonable request.

Keywords

amino acids, films, interfacial assembly, liquid–liquid separation, perfluorocarbon

Received: May 4, 2021
Revised: June 2, 2021
Published online: June 23, 2021

[1] S. Sarkar, S. Das, S. Dagar, M. P. Joshi, C. V. Mungi, A. A. Sawant, G. M. Patki, S. Rajamani, *J. Membr. Biol.* **2020**, *253*, 589.
[2] M.-T. Wei, S. Elbaum-Garfinkle, A. S. Holehouse, C. C.-H. Chen, M. Feric, C. B. Arnold, R. D. Priestley, R. V. Pappu, C. P. Brangwynne, *Nat. Chem.* **2017**, *9*, 1118.
[3] V. N. I. Uversky, *Curr. Opin. Struct. Biol.* **2017**, *44*, 18.
[4] S. Brocca, R. Grandori, S. Longhi, V. Uversky, *Int. J. Mol. Sci.* **2020**, *21*, 9045.
[5] S. Elbaum-Garfinkle, *J. Biol. Chem.* **2019**, *294*, 7160.
[6] Q. Li, X. Peng, Y. Li, W. Tang, J. Zhu, J. Huang, Y. Qi, Z. Zhang, *Nucleic Acids Res.* **2020**, *48*, D320.
[7] Y.-H. Lin, J. D. Forman-Kay, H. S. Chan, *Biochemistry* **2018**, *57*, 2499.
[8] E. W. Martin, T. Mittag, *Biochemistry* **2018**, *57*, 2478.
[9] S. Alberti, A. Gladfelter, T. Mittag, *Cell* **2019**, *176*, 419.
[10] M. Abbas, W. P. Lipiński, J. Wang, E. Spruijt, *Chem. Soc. Rev.* **2021**, *50*, 3690.
[11] A. Molliex, J. Temirov, J. Lee, M. Coughlin, A. P. Kanagaraj, H. J. Kim, T. Mittag, J. P. Taylor, *Cell* **2015**, *163*, 123.
[12] S. F. Banani, H. O. Lee, A. A. Hyman, M. K. B. Rosen, *Nat. Rev. Mol. Cell Biol.* **2017**, *18*, 285.
[13] J. N. Sloand, A. M. Miller, S. H. Medina, *Pept. Sci.* **2020**, *113*, e24184.

[14] Y. Zhang, H. Gu, Z. Yang, B. Xu, *J. Am. Chem. Soc.* **2003**, *125*, 13680.
[15] A. N. Shy, B. J. Kim, B. Xu, *Matter* **2019**, *1*, 1127.
[16] R. Orbach, I. Mironi-Harpaz, L. Adler-Abramovich, E. Mossou, E. P. Mitchell, V. T. Forsyth, E. Gazit, D. Seliktar, *Langmuir* **2012**, *28*, 2015.
[17] A. K. Das, R. Collins, R. V. Ulijn, *Small* **2008**, *4*, 279.
[18] A. Rajbhandary, W. W. Brennessel, B. L. Nilsson, *Cryst. Growth Des.* **2018**, *18*, 623.
[19] D. M. Ryan, T. M. Doran, S. B. Anderson, B. L. Nilsson, *Langmuir* **2011**, *27*, 4029.
[20] D. M. Ryan, S. B. Anderson, F. T. Senguen, R. E. Youngman, B. L. Nilsson, *Soft Matter* **2010**, *6*, 475.
[21] S. Fleming, S. Debnath, P. W. J. M. Frederix, T. Tuttle, R. V. Ulijn, *Chem. Commun.* **2013**, *49*, 10587.
[22] P. W. J. M. Frederix, G. G. Scott, Y. M. Abul-Haija, D. Kalafatovic, C. G. Pappas, N. Javid, N. T. Hunt, R. V. Ulijn, T. Tuttle, *Nat. Chem.* **2015**, *7*, 30.
[23] A. Brito, Y. M. Abul-Haija, D. S. da Costa, R. Novoa-Carballal, R. L. Reis, R. V. Ulijn, R. A. Pires, I. Pashkuleva, *Chem. Sci.* **2019**, *10*, 2385.
[24] *FACT SHEET: PFOA & PFOS Drinking Water Health Advisories, EPA 800-F-16-003*, **2016**.
[25] M. W. Sima, P. R. Jaffé, *Sci. Total Environ.* **2021**, *757*, 143793.
[26] R. Naidu, P. Nadebaum, C. Fang, I. Cousins, K. Pennell, J. Conder, C. J. Newell, D. Longpré, S. Warner, N. D. Crosbie, A. Surapaneni, D. Bekele, R. Spiese, T. Bradshaw, D. Slee, Y. Liu, F. Qi, M. Mallavarapu, L. Duan, L. McLeod, M. Bowman, B. Richmond, P. Srivastava, S. Chadalavada, A. Umeh, B. Biswas, A. Barclay, J. Simon, *Environ. Technol. Innovation* **2020**, *19*, 100915.
[27] N. Bolan, B. Sarkar, Y. Yan, Q. Li, H. Wijesekara, K. Kannan, D. C. W. Tsang, M. Schauerte, J. Bosch, H. Noll, Y. S. Ok, K. Scheckel, J. Kumpiene, K. Gobindlal, M. Kah, J. Sperry, M. B. Kirkham, H. Wang, Y. F. Tsang, D. Hou, J. Rinklebe, *J. Hazard. Mater.* **2021**, *401*, 123892.
[28] R. M. Vernon, P. A. Chong, B. Tsang, T. H. Kim, A. Bah, P. Farber, H. Lin, J. D. Forman-Kay, *eLife* **2018**, *7*, e31486.
[29] H.-R. Li, W. - C. Chiang, P.-C. Chou, W.-J. Wang, J. T. A. R. Huang, *J. Biol. Chem.* **2018**, *293*, 6090.
[30] A. M. Smith, R. J. Williams, C. Tang, P. Coppo, R. F. Collins, M. L. Turner, A. Saiani, R. V. Ulijn, *Adv. Mater.* **2008**, *20*, 37.
[31] M. Biancalana, S. Koide, *Biochim. Biophys. Acta, Proteins Proteomics* **2010**, *1804*, 1405.
[32] A. Rajbhandary, D. M. Raymond, B. L. Nilsson, *Langmuir* **2017**, *33*, 5803.
[33] A. Rajbhandary, B. L. Nilsson, *Pept. Sci.* **2017**, *108*, e22994.
[34] D. M. Murali, G. Shanmugam, *New J. Chem.* **2019**, *43*, 12396.
[35] V. Castelletto, C. M. Moulton, G. Cheng, I. W. Hamley, M. R. Hicks, A. Rodger, D. E. López-Pérez, G. Revilla-López, C. Alemán, *Soft Matter* **2011**, *7*, 11405.
[36] R. C. Lewis, L. E. Johns, J. D. Meeker, *Int. J. Environ. Res. Public Health* **2015**, *12*, 6098.
[37] C. C. Bach, A. Vested, K. T. Jørgensen, J. P. E. Bonde, T. B. Henriksen, G. Toft, *Crit. Rev. Toxicol.* **2016**, *46*, 735.
[38] G. Liu, K. Dhana, J. D. Furtado, J. Rood, G. Zong, L. Liang, L. Qi, G. A. Bray, L. DeJonge, B. Coull, P. Grandjean, Q. Sun, *PLoS Med.* **2018**, *15*, e1002502.
[39] J. M. Braun, *Nat. Rev. Endocrinol.* **2017**, *13*, 161.
[40] K. Kielsen, Z. Shamim, L. P. Ryder, F. Nielsen, P. Grandjean, E. Budtz-Jørgensen, C. Heilmann, *J. Immunotoxicol.* **2016**, *13*, 270.
[41] Y. Fang, A. Ellis, Y. J. Choi, T. H. Boyer, C. P. Higgins, C. E. Schaefer, T. J. Strathmann, *Environ. Sci. Technol.* **2021**, *55*, 5001.
[42] U. Rao, Y. Su, C. M. Khor, B. Jung, S. Ma, D. M. Cwiertny, B. M. Wong, D. Jassby, *Environ. Sci. Technol.* **2020**, *54*, 10668.
[43] E. Kumarasamy, I. M. Manning, L. B. Collins, O. Coronell, F. A. Leibfarth, *ACS Cent. Sci.* **2020**, *6*, 487.
[44] W. Ji, L. Xiao, Y. Ling, C. Ching, M. Matsumoto, R. P. Bisbey, D. E. Helbling, W. R. Dichtel, *J. Am. Chem. Soc.* **2018**, *140*, 12677.
[45] J. G. Sepulvado, A. C. Blaine, L. S. Hundal, C. P. Higgins, *Environ. Sci. Technol.* **2011**, *45*, 8106.
[46] J. W. Washington, H. Yoo, J. J. Ellington, T. M. Jenkins, E. L. Libelo, *Environ. Sci. Technol.* **2010**, *44*, 8390.
[47] R. Das, B. Gayakvad, S. D. Shinde, J. Rani, A. Jain, B. Sahu, *ACS Appl. Bio Mater.* **2020**, *3*, 5474.
[48] Y. Yu, K. Zhang, Z. Li, C. Ren, J. Chen, Y.-H. Lin, J. Liu, Y. Men, *Environ. Sci. Technol.* **2020**, *54*, 14393.
[49] S. Huang, P. R. Jaffé, *Environ. Sci. Technol.* **2019**, *53*, 11410.